Materials and Design 194 (2020) 108845

Contents lists available at ScienceDirect

Materials and Design

journal homepage: www.elsevier.com/locate/matdes

Comprehensive assessment of the printability of CoNiCrFeMn in Laser Powder Bed Fusion

Bogdan Dovgyy [a,*], Alessandro Piglione [a], Paul A. Hooper [b], Minh-Son Pham [a]

[a] Department of Materials, Imperial College London, SW7 2AZ, UK
[b] Department of Mechanical Engineering, Imperial College London, SW7 2AZ, UK

HIGHLIGHTS

- Highly consolidated CoNiCrFeMn is achieved in Laser Powder Bed Fusion using an energy density between 62.7 and 109.8 kJ/m^3
- Scanning strategy has a significant impact on consolidation of CoNiCrFeMn in Laser Powder Bed Fusion.
- Microstructure and plastic anisotropy are governed by scanning strategy, in particular the angle of rotation between layers.
- CoNiCrFeMn fabricated via Laser Powder Bed Fusion has excellent strength and good ductility.

GRAPHICAL ABSTRACT

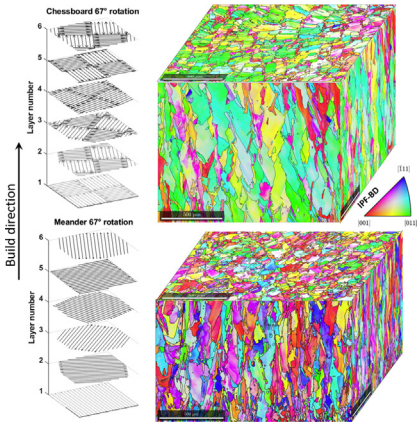

ARTICLE INFO

Article history:
Received 6 January 2020
Received in revised form 6 May 2020
Accepted 31 May 2020
Available online 13 June 2020

Keywords:
Additive manufacturing
Laser Powder Bed Fusion
High entropy alloy
3D print
Texture
Mechanical properties

ABSTRACT

This study assesses the printability including the consolidation, solidification microstructure, and mechanical properties of the CoCrFeMnNi high entropy alloy fabricated by Laser Powder Bed Fusion. A range of print parameters was used for a comprehensive assessment of printability, providing a basis to establish the relationship between process, microstructure, and mechanical properties. The study demonstrates a high relative density of the alloy fabricated with energy density in the range 62.7–109.8 J/mm^3. It is shown that the scan strategy plays an important role in consolidation. For the same energy density, the rotation of 67° between two consecutive layers tends to yield higher consolidation than other considered strategies. Moreover, the scan strategy is found to be most influential in microstructure development. The scan strategy rotation angle controls the extent to which epitaxial growth can occur, and hence the crystallographic texture and the grain morphology. Amongst four considered strategies, the 0°- and 90°-rotation meander led to the strongest preferred texture while the 67°-rotation resulted in weaker texture. The 67°-rotation strategies led to broadened grains with lower aspect ratios. The understanding of texture and grain size provides explanations to the observed mechanical properties (such as flow stress and plastic anisotropy) of the alloy.

1. Introduction

Additive manufacturing (AM) technologies show great potential in fabricating components with high geometrical flexibility, reduced lead

* Corresponding author.
E-mail address: bogdan.dovgyy13@imperial.ac.uk (B. Dovgyy).

https://doi.org/10.1016/j.matdes.2020.108845

time [1], and is a key enabler for the development of advanced materials such as architected materials [2]. Moreover, the nature of the process allows to locally tailor the microstructure (namely the solidification structure, grain morphology (shape and size) and the grain crystallographic orientation, i.e. texture) and, hence, the mechanical properties. It has been well documented that the microstructure and mechanical properties of the AM builds are very anisotropic and strongly influenced by the process parameters [3–7]. However, in order to achieve maximum consolidation, an optimal processing window has to be used. This means that such optimized parameters as laser power, scan speed, and hatch spacing are usually kept constant throughout the build/material. This brings more interest to the scan strategy as a way to modify the properties of the component while keeping the aforementioned parameters constant. Shi-Hai and colleagues [8] recently investigated the effect of scan strategy on the texture in a face centred cubic (FCC) Ni—Mo alloy. They reported that the degree of epitaxial growth, and therefore texture, can be controlled by manipulating the scan strategy. Livescu et al. [7] showed that the scan strategy can significantly affect the texture along the build direction in pure tantalum. The maximum multiple uniform density (MUD) index, a quantitative measure of texture, changed by a factor of about 3 (from 32 to 12) as the stripe width was reduced from 5 mm to 2 mm. Geiger and co-workers [4] showed on IN738LC that by changing the angle of rotation between the layers (from 90° rotation to 67°) it could lead up to a 25% change in the apparent Young modulus. Thijs et al. [6] qualitatively demonstrated on pure body centred cubic (BCC) tantalum that the grain morphology and texture affect the Taylor factor $\overline{M}$ and, hence the yield stress of the material in AM builds. The elongated nature of grains along the build direction and the orientation of the {110}⟨111⟩ and {112}⟨111⟩ slip systems with respect to the build direction resulted in a 15% increase in yield stress along build direction as compared to the yield stress in the transverse direction (predicted using viscoplastic self-consistent (VPSC) model). A recent review by Kok et al. [9] shows that in Ti-64, IN178, AlSi10Mg, and CoCrMo alloys the anisotropy of mechanical properties is significantly influenced by the process parameters and physical properties of the material (thermal conductivity and crystal structure). It was concluded that grain morphology and texture play a significant role in anisotropy [10]. Therefore, it is important to understand the mechanisms of texture evolution and grain growth and their effect on microstructures and mechanical properties of additively manufactured components made from various materials.

Despite many studies assessing the printability of existing alloys (such as 316L steel, Ti6Al4V, Al10SiMg), metallurgical issues in 3D printing of these alloys remain difficult to be solved as these materials were developed for slow cooling processes such as casting. Therefore, there has been an increasing interest in developing and 3D printing of new materials. High entropy alloys (HEAs) are promising candidates in this regard. Several groups have investigated the mechanical properties, microstructure, and printability of equimolar CoCrFeMnNi HEA through various AM processes [11–16]. Li et al. [11] investigated the influence of the process parameters on porosity, microstructures, and mechanical properties using Laser Powder Bed Fusion (LPBF). Wang et al. [16] performed a similar investigation with an alloy manufactured via Electron Beam Melting (EBM). Oliveira et al. [13] performed gas tungsten arc welding of a rolled version of the alloy showing good suitability of this process to achieve defect-free welds with good ductility. In the view of commercial applications of this alloy Guo et al. [14] studied post-processing routes to achieve a smooth surface finish of as-built material manufactured via LPBF. This overwhelming interest in additively manufactured CoCrFeMnNi alloy sets the need to establish a better understanding of the relation between the process parameters, microstructure, and mechanical properties (in particular the plastic anisotropy).

Our previous study showed that this alloy has a high printability [12] thanks to the material microstructure. The material develops a stable FCC single phase structure upon rapid cooling [17], eliminating the risk to form cracks associated with phase transformation during thermal cycles. High melting temperature oxides can prevent the flow of molten metal, resulting in an increased risk of forming the lack of fusion porosity. Therefore, a high concentration of Cr in the alloy results in high oxidation resistance, minimizing the formation of porosity associated with oxidation, and thereby improving consolidation. The low thermal expansion coefficient minimizes internal stresses [18], while a relatively low freezing range helps in preventing solidification cracking. This makes this alloy an excellent candidate to be fabricated by AM with a wide processing window. In this study, we build a better understanding of the processing map; establish the relationship between process parameters, microstructure, and mechanical properties; expand the fundamental understanding of the local and macroscopic crystallographic textures formed in the LPBF process. In particular, the effect on the microstructure of various process parameters, and most importantly the scan strategy, is investigated. Materials texture and mechanical properties are then measured and related to the process parameters.

2. Materials and methods

Pre-alloyed CoCrFeMnNi powder was provided by HC Starck Surface Technology & Ceramic Powders GmbH. The composition of the powder after atomisation was nearly equiatomic. This was confirmed by energy dispersive X-ray spectroscopy (EDX) analyses (see Table A1 in Appendix), conducted using a Zeiss Auriga scanning electron microscope (SEM) operating at 20 kV. To obtain the particle size distribution of the metallic powder, SEM analyses were carried out using a JEOL 5610LV: 20 images were taken at 300× magnification and subsequently analysed using ImageJ. The particle size distribution of the HEA powder is shown in Fig. 1. The samples of the current work were fabricated by a LPBF process under argon atmosphere using a Renishaw AM250 equipped with a modulated InGaAs laser emitting at 905 nm. Unlike most LPBF systems, Renishaw uses a modulated beam, where the laser is activated for a defined time period (exposure time) at predefined distance intervals (point distance) along the scan path (hatch lines). A standard set of printing parameters was defined as: a laser power of 200 W, a hatch spacing of 85 μm, an exposure time of 80 μs, a point distance of 60 μm, a layer height of 50 μm, a laser beam spot size of 65 μm and a bidirectional scan strategy with 67° rotation between consecutive layers (these parameters were optimised in-house for LPBF of 316L stainless steel and were used here as the starting point of standard process parameters because the two materials are of the Fe-Cr-Ni alloy system and have the same crystal structure - face-centred cubic). To investigate grain growth in rapid cooling, single track samples (the

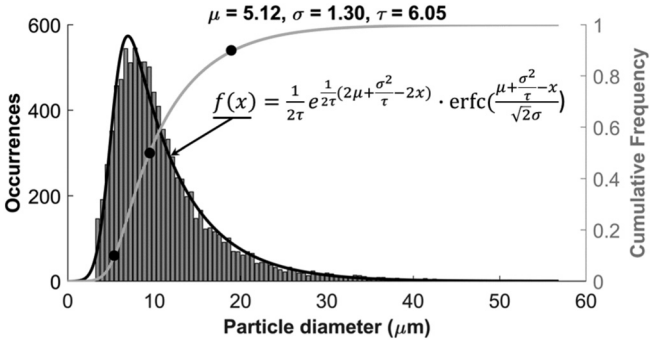

Fig. 1. Cumulative and frequency particle size distribution of the HEA powder with fitted exponentially modified Gaussian curve (distribution function and fit parameters μ (mean), σ (standard deviation) and τ (relaxation time) are displayed in the middle and at the top of the figure, respectively) and indicated quantiles at 0.1, 0.5 and 0.9 (black circle markers).

laser scans 1 hatch line on the substrate with 1 layer thick powder deposit) were produced using the standard process parameters. To study the influence of individual printing parameters on the quality of builds, selected parameters were varied from the standard set, see Fig. 2 (cubes of $10 \times 10 \times 10\ mm^3$ were printed in a 3×3 matrix, with sample ID corresponding to the location of the sample on the build plate). In particular, the exposure times were varied for strategies 11, 12, and 13 (100, 120, and 140 μs, respectively). The scan strategy was varied for samples 21, 22, and 23; in particular a bi-directional scan strategy was used for sample 21, 23, 31, 32, and 33; and a chessboard scan strategy (i.e. each layer subdivided into squared domains with 90° rotation of scanning direction between two adjoining domains) for sample 22. In strategies 21 and 23, the rotation angle between layers was changed to 0° (no rotation) and 90°, respectively. The same scan strategy (bidirectional with 67° rotation between layers) was used but hatch spacing was varied for 31, 32, and 33 (60, 85, and 110 μm, respectively). All considered sets of parameters are shown and summarised in Fig. 2 and Table 1. Table 1 also shows volumetric energy density, a common metric used to optimise consolidation, for each set of parameters. Energy density is calculated using Eq. (1).

$$E_\rho = \frac{P}{v \cdot h \cdot t} \tag{1}$$

where P, v, h and t denote laser power, scan speed, hatch spacing, and layer thickness, respectively.

The consolidation of the HEA fabricated by Laser Powder Bed Fusion is reflected via the relative density, which is calculated as a ratio of experimentally measured densities to the theoretical density. The theoretical density of the HEA was calculated using Eq. (2).

$$\rho = \frac{n * A}{V_c * N_A} \tag{2}$$

where n is the number of atoms per unit cell ($n = 4$ for FCC lattice), V_c the volume of a lattice unit cell (derived from the calculated lattice parameter $V_c = a^3$) and N_A is Avogadro constant. A is the average atomic weight per lattice site calculated from Eq. (3)

$$A = \frac{1}{m}\sum_i^m W_i * c_i \tag{3}$$

where m is the number of elements in the alloy, W_i the atomic weight of element i and c_i the atomic fraction of element i (obtained by EDX mapping of $1 \times 1\ mm^2$ region of an as-printed sample for 1.5 h with total counts reaching 12 million). The obtained theoretical density, together with the density values obtained via Archimedes' principle measurements and optical density measurements, were used to calculate the relative density of the samples. The error bars used in the figures were derived from the calculated uncertainties of the measurements according to ISO 21748:2017.

Both as-received powder and AM builds were analysed by X-ray diffraction (XRD) using a Bruker D2 Phaser using the Cu Kα radiation (wavelength of 1.5406 Å), with a 2θ angle ranging from 9° to 99°, an angle increment of 0.036° and a timestep of 0.5 s. This analysis was aimed at identifying the phases present and at measuring the lattice

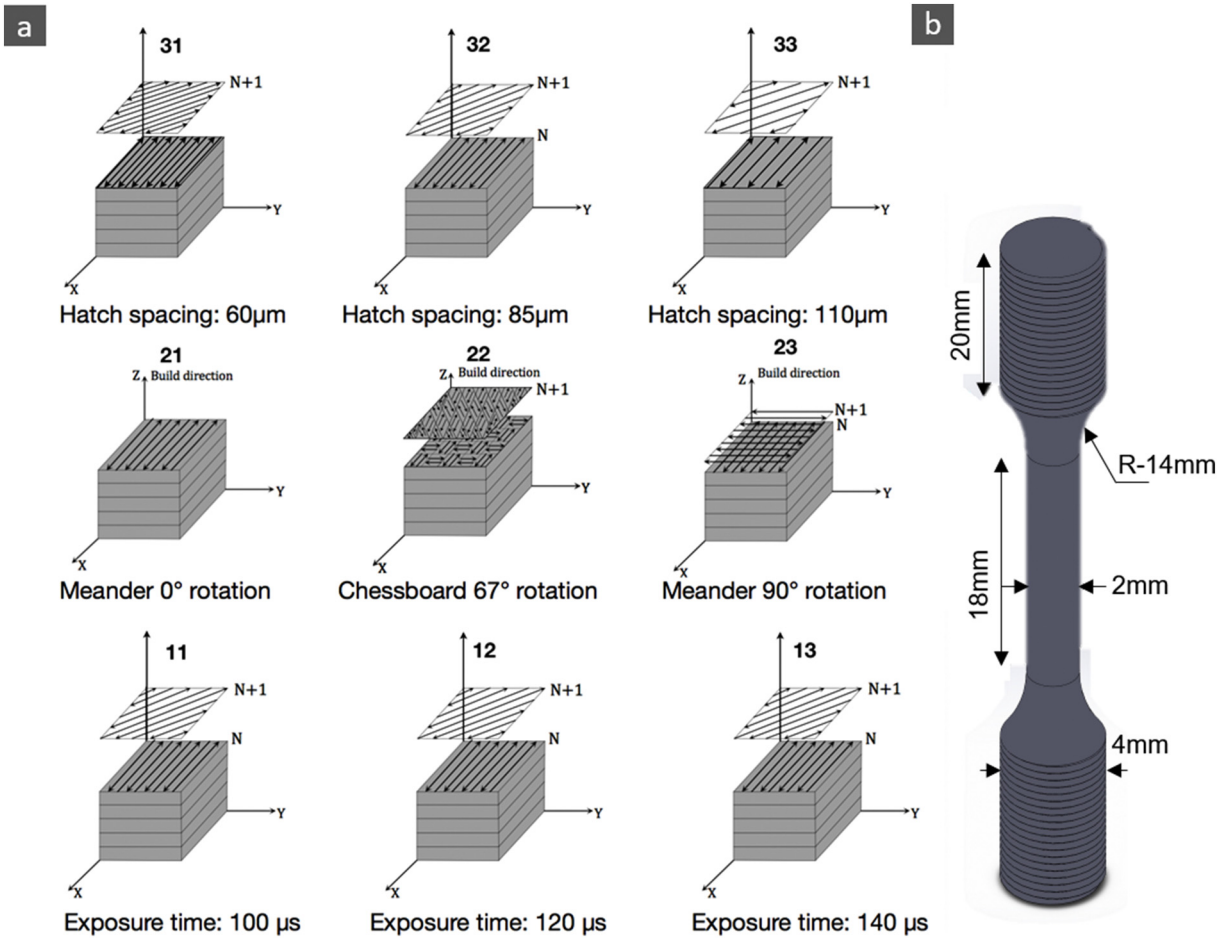

Fig. 2. (a) Different printing strategies used to fabricate the HEA samples with indicated variation from the standard parameters (N and N + 1 denote the layer N and the layer N + 1, respectively). (b) The geometry of the cylindrical tensile test piece.

Table 1
Print parameters used for the investigation.

Sample	Exposure time (μs)	Point distance (μm)	Hatch spacing (μm)	Scan strategy	Layer rotation (°)	Effective speed (m/s)	Energy density ($J \cdot mm^{-3}$)
11	100	60	85	Meander	67	0.60	78.4
12	120	60	85	Meander	67	0.50	94.1
13	140	60	85	Meander	67	0.43	109.8
21	80	60	85	Meander	0	0.75	62.7
22	80	60	85	Chessboard	67	0.75	62.7
23	80	60	85	Meander	90	0.75	62.7
31	80	60	60	Meander	67	0.75	88.9
32	80	60	85	Meander	67	0.75	62.7
33	80	60	110	Meander	67	0.75	48.5
Tensile	80	60	85	Chessboard	67	0.75	62.7
Single track	80	60	85	Line	N/A	0.75	62.7

parameter. The sample coordinates were defined with Z being parallel to the build direction (BD), X being parallel to a scan direction and Y being perpendicular to both X and Z. Samples were then sectioned into 3 pieces to evaluate hardness and microstructural variations along the build direction (X or Y section) and perpendicular to the BD (Z-section). Hardness measurements (HV2) were carried out applying a 2 kg load for 10 s. At least 15 indentations were made in a regular array for each section. In addition to cubic builds, cylindrical test pieces (dimensions are shown in Fig. 2b) were printed horizontally and vertically (i.e., with their longitudinal direction perpendicular and parallel to the build direction, respectively) using strategy 22. The cylindrical test pieces were subjected to tensile tests at room temperature, using a strain rate of 10^{-3} s^{-1}. The tensile tests were performed in accordance to ISO 6892-1:2019. The strain was measured using either an extensometer or by digital image correlation (DIC) in identical test conditions. The DIC sample was primed in white paint, while black spray paint was used to produce the speckle pattern. To capture the initial deformation in the elastic region, the DIC camera was set to a rate of 1 frame/s. The image sequence for the DIC was analysed using the GOM Correlate software.

As-built and deformed samples were ground using SiC papers with P-grades of 800, 1200, 2400, and 4000. Subsequently, specimens were polished using a colloidal silica suspension with particles of 0.04 μm mixed with distilled water in 50:50 concentration ratio. To reveal the fine microstructure, the polished samples were electrochemically etched in 10% Oxalic acid (in H_2O) at 2.5 V for 90 s. Microstructural observations were performed using a Zeiss Sigma 300 and a Zeiss Auriga SEMs, both equipped with a high-resolution electron backscatter diffraction (EBSD) detector. The MTEX toolbox [19] was used to analyse the obtained EBSD data. Samples for (Scanning) Transmission Electron Microscopy ((S)TEM) were prepared by electropolishing 3 mm disks using a solution of 10% perchloric acid in methanol, applying a voltage of 20 V at −20 °C. (S)TEM was performed using a JEOL 2100F TEM equipped with an Oxford Instruments EDX detector.

3. Results and discussions

3.1. Print parameters and consolidation

The effectiveness of the energy density to predict the consolidation is still being disputed because the density does not completely reflect the complex physical phenomena occurring during melting and solidification in LPBF process, however, this metric provides a good start for process parameter optimisation if used carefully [20,21]. In this study, print strategies with energy density above 62.7 Jmm^{-3} provided samples with very good consolidation (Fig. 3a). Energy densities above the threshold are believed to generate a sufficiently big pool of molten metal to fill the gap between melt tracks to minimise the formation of lack-of-fusion porosity. However, if the energy density is too excessive, it can increase the vaporisation and keyholes, inreasing gas-entrapped and keyhole porosity, i.e. lowering the consolidation of the alloy in LPBF. Therefore, there is an upper bound of the volumetric energy density which was found for this alloy to be 109.8 Jmm^{-3}. It is worth noting that a large measurement error in sample 12 (energy density of 94.1 Jmm^{-3}) was associated with the small size of the sample (section) used for Archimedes density measurement. This inevitably influenced the uncertainty in weight measurement. The optical density measurements showed generally higher apparent densities compared to the values obtained via Archimedes' principle. However, optical measurements are strongly dependent on the location of the section, and hence less representative of the density of each sample. The Archimedes measurements agree with the study performed by Li et al. [11] on the same HEA, showing that minimum energy density to obtain highly dense parts is around 60 Jmm^{-3}. Interestingly, at the same energy

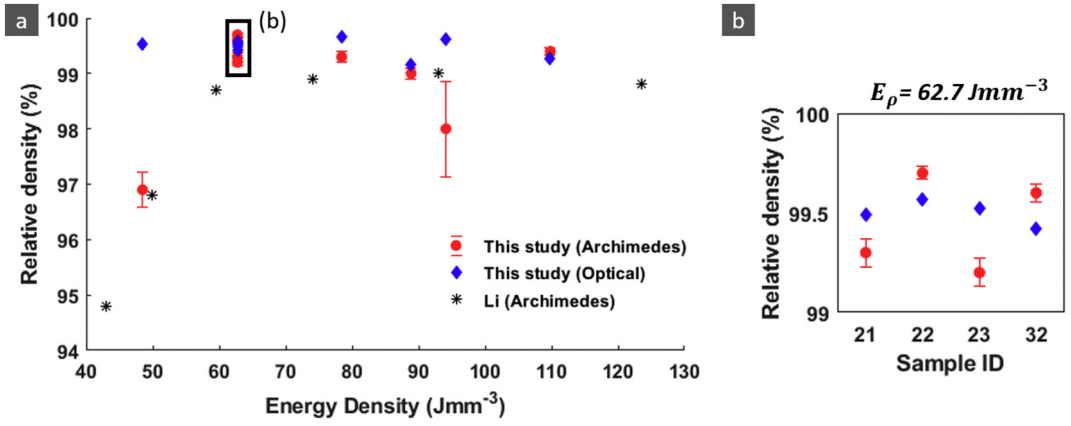

Fig. 3. (a) Relative densities of samples measured using Archimedes' principle and optical measurements in this study and a study performed by Li et al. [11]. with respect to the energy density used for printing. (b) Differences between samples at the same energy density (marked by a black rectangle in (a)).

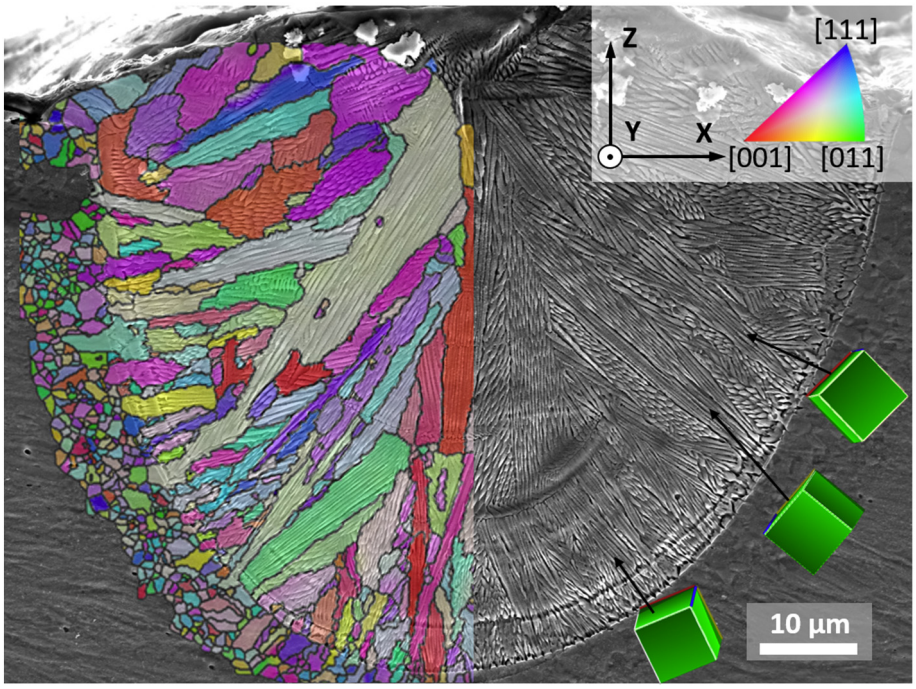

Fig. 4. An overlay of an EBSD IPF-Z map and an SEM image of a section perpendicular to a HEA single track. Green cubes at the bottom right show the crystallographic orientation of the cells in the regions indicated by the black arrows. (For interpretation of the references to color in this figure legend, the reader is referred to the web version of this article.)

density ($E_\rho = 62.7\ Jmm^{-3}$), different scan strategies resulted in different consolidation, Fig. 3(b). Archimedes measurement clearly shows that a 67° rotation between consecutive layers increases the consolidation: Samples 22 and 32 (chessboard and meander strategies, respectively, with 67° rotation between layers) show higher relative density (i.e. consolidation) compared to samples 21 and 23 (meander with 0° and 90° rotation between layers, respectively). This is believed to occur due to the rotation angle between layers of deposition. Unlike the sample 21, in which deposition tracks should theoretically be well aligned on top of the beneath tracks, the 67° rotation increases the crossing between newly and pre-deposited tracks, helping to eliminate lack-of-fusion pores that formed between tracks in the previous layers, hence increasing the consolidation. In addition, the deposition in sample 23 with 90° rotation is repeated on the same location only after every 2 layers which is much fewer than that associated with the rotation of 67°.

3.2. Process parameters and microstructure

3.2.1. Microstructure in the single track

Microstructure development during solidification is governed by the nucleation and competitive growth of crystals. In fusion-based additive manufacturing processes, the molten metal is deposited on an existing solid which is usually of the same composition (except for the first few layers of deposition when a different material is used as a substrate). Therefore, the driving force for nucleation is nearly zero (Appendix, section A). In addition, the substrate in Laser Powder Bed Fusion is usually cold, leading to extremely high thermal gradient and high velocity of liquidus isotherm. Consequently, epitaxial columnar growth is dominant in microstructure development in fusion AM [22]. This was confirmed when a single track of the HEA was deposited on a solid 316L stainless steel substrate [12] (Fig. 4). Cells grew epitaxially from existing grains in the substrate, with both the cell axis and one ⟨100⟩ direction nearly perpendicular to the fusion line (as shown by the cubes at the bottom right of Fig. 4), confirming that cells grow following the local maximum heat flux direction along one of their ⟨100⟩ preferred growth directions which is in agreement with previous studies reporting that ⟨100⟩ is the preferred growth direction for cubic crystals including face centred cubic and body centred cubic metals [23–25].

3.2.2. Microstructure in multi-layer depositions

SEM micrographs of etched samples revealed a typical 'fish scale' microstructure associated with the presence of fusion lines (Fig. 5a) that is very commonly found in AM alloys [11]. The 'fish scale' microstructure is formed thanks to variations in local chemical composition and solidification microstructure along the boundaries of the solidified weld bead. Each bead contains fine cells (Fig. 5b). The cell diameter ranged between 300 nm and 1000 nm, depending on the location within the melt pool and on the processing parameters. TEM investigations showed that cell interiors were mostly dislocation free, while high dislocation densities were observed at cell boundaries (Fig. 5c and d), in agreement with previous TEM investigations of printed FCC metals [26,27]. Dislocations within cell boundaries were tangled and can act as obstacles to the movement of dislocations inside cells. The misorientation between solidification cells was about 1° to 2°. Fig. 5d shows the presence of some precipitates (marked in Fig. 5d using circles and squares), with sizes of 80± 30 nm. These precipitates formed both inside cells and on the cell boundaries (highlighted by solid and dashed lines in Fig. 5d, respectively). STEM-EDX (Appendix, Fig. B1) revealed increased oxygen level in such precipitates. This suggests that these precipitates formed due to oxidation during the LPBF process.

The melt pools' depth was found to increase with increasing exposure time due to the increase in the energy density, while the regularity of the arrangement of the melt pools strongly depended on the scan pattern. For example, a meander pattern with 0° rotation resulted in an ordered arrangement of melt pools, stacked in vertical columns along the build direction (Fig. 5e); on the other hand, a meander pattern with 67° rotation resulted in an apparently disordered arrangement of melt pools, Fig. 5f, the appearance of which is dependent on the orientation of the section with respect to the build and scanning directions.

3.2.3. Scan strategy and crystallographic texture

It was found that variations in beam point distance and exposure time only had a negligible effect on the solidification microstructure in

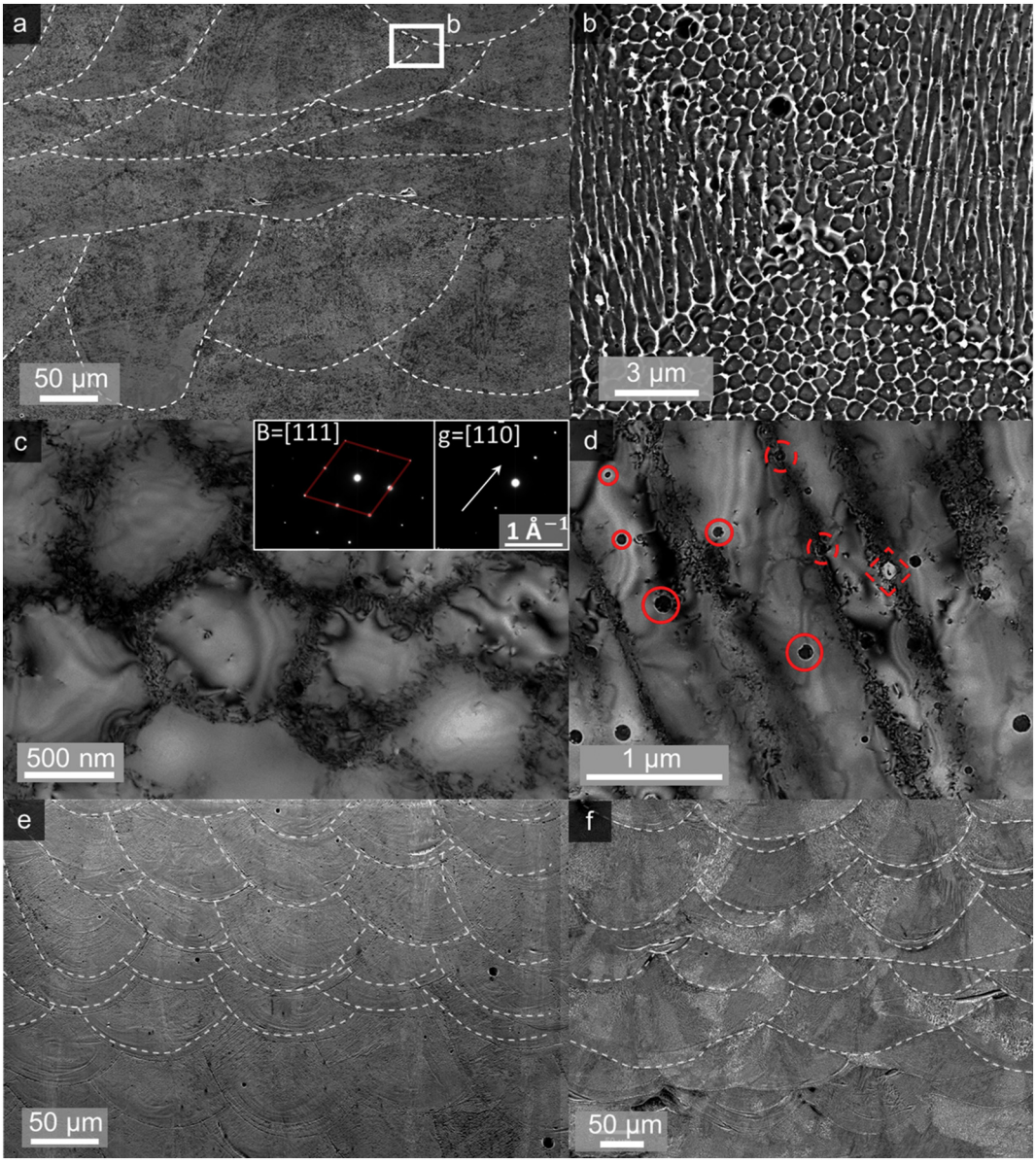

Fig. 5. SEM micrographs showing (a) the "fish scale" microstructure of melt pool arrangement in the HEA fabricated using the 'chessboard' pattern (strategy 22), (b) cells at a junction of three weld beads in a magnified region enclosed by a rectangle in (a); Bright field TEM of a 3 sample in (a) imaged in a two-beam condition - (c) (see insert for zone axis and g vector) and in multibeam condition - (d), note that different precipitates are highlighted by circles and squares, while dashed and solid lines represent the position at the cell boundaries and in the bulk, respectively; (e) and (f) show the arrangement of melt pools in the HEA fabricated with strategies 21 (meander – 0° rotation) and 32 (meander – 90° rotation), respectively.

highly dense samples (>99%). The solidification microstructure (such as planar, columnar cells/dendrites, and equiaxed dendrites) is mainly governed by solidification velocity and thermal gradient [24]. The variation in point distance and exposure time within the considered processing window probably did not result in substantial changes in the solidification velocity and thermal gradient to cause significant alterations in the solidification microstructure. However, Fig. 6 shows that the variation in scan strategy results in significant changes to the microstructure of the HEA alloy, and in particular to grain morphologies and crystallographic orientations. The left column of Fig. 6 shows that the appearance of the microstructure observed in the Z sections (perpendicular to the build direction - Fig. 6a, c, e, g) differs significantly from that observed in X sections, i.e. parallel to the build direction (right column - Fig. 6b, d, f, h). The grain structures observed in the Z sections resemble the scan strategy adopted. This is particularly clear for strategy 21 (meander pattern with 0° rotation), which resulted in a grain microstructure that resembles the deposition tracks along the sole scanning direction (the X direction), Fig. 6a. In particular, the EBSD map revealed lines of small grains aligned parallel to the scanning direction. These grains are located along the centreline of deposition tracks. Similarly, the strategy 23 (meander with 90° rotation) leads to a square pattern of grain microstructure, Fig. 6e; this is due to the fact that the X and Y directions were the scanning direction on alternating layers, and that they were perpendicular to one another.

Since the heat flux is a function of the beam direction (and hence of the scan pattern), it is no surprise that the scan patterns have profound influences on the final microstructure of HEA builds, as seen in Fig. 6. If the flow of molten metal within each melt pool is in steady state, a simplified assumption can be made that the heat flux distribution in melt pools is repeated for each melt pool. The variation in the scanning direction, however, changes the melt pool orientation. Hence, the angle between consecutive layers plays a key role in the epitaxial growth in AM, as it sets the orientation of the new heat flux with respect to existing cells (epitaxial growth and grain competition mechanisms are described in the Appendix). With the energy density of the standard parameters used in this work, a new melt pool of HEA was observed to

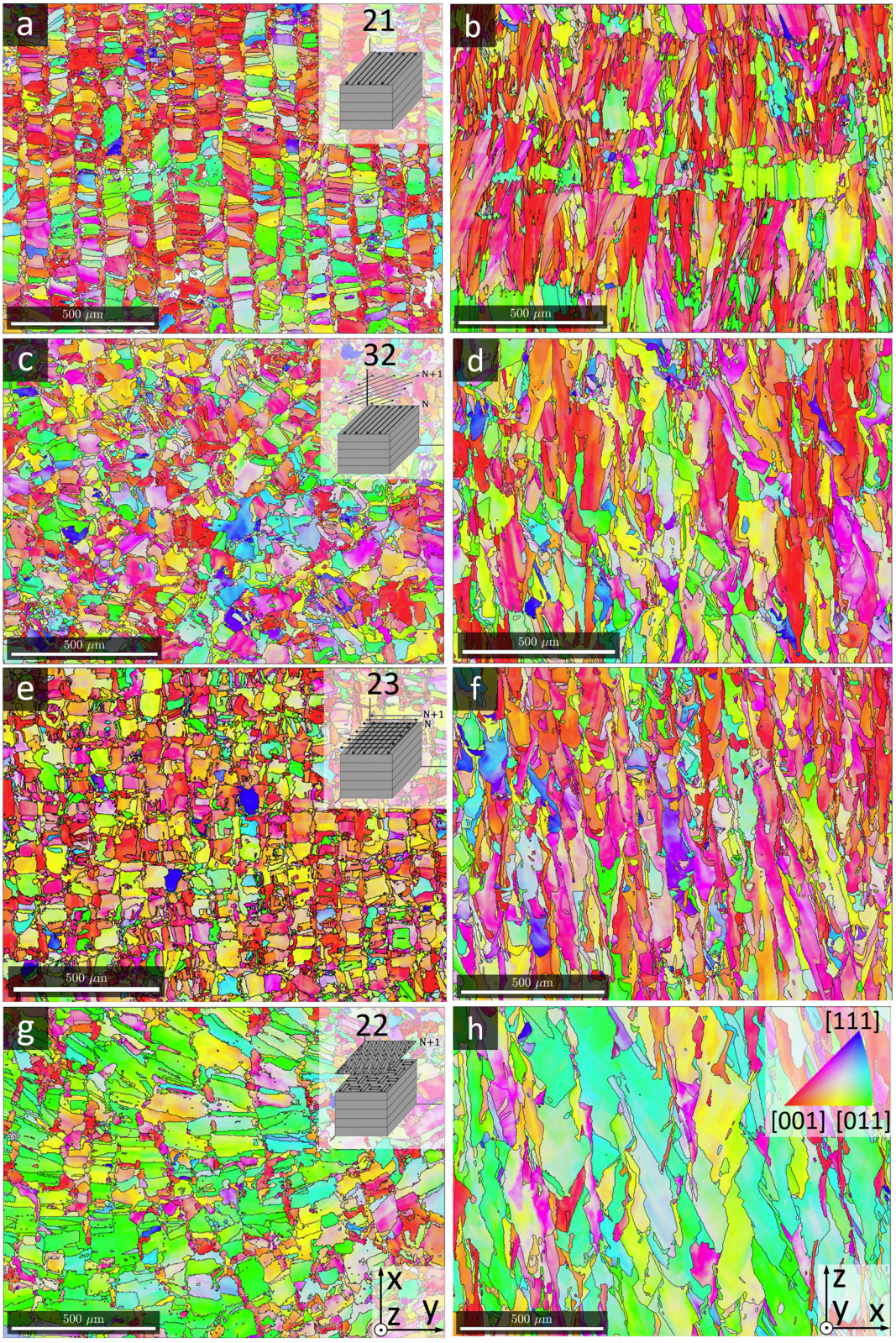

Fig. 6. EBSD IPF-Z maps (Z = build direction) of samples fabricated with selected printing strategies from the top (left column) and the side view (right column). (a), (b) – strategy 21; (c), (d) – strategy 32; (e), (f) – strategy 23; (g), (h) – strategy 22.

penetrate up to 4 layers of the previously deposited material (observed by measuring and analysing dimensions of the melt tracks on the top-most layer). Thus, the crystal orientations of cells in the newest melt pool were affected by those in 1–4 previous layers thanks to epitaxial growth. Fig. 7 shows the overlay of the scanning directions of six consecutive layers for the three different strategies used in this work. It is possible to observe that the microstructures observed in Fig. 6 for the *Z*-cuts clearly resemble the top views of the corresponding scan patterns (Fig. 7b1–3), confirming the observations shown in the left column of Fig. 6.

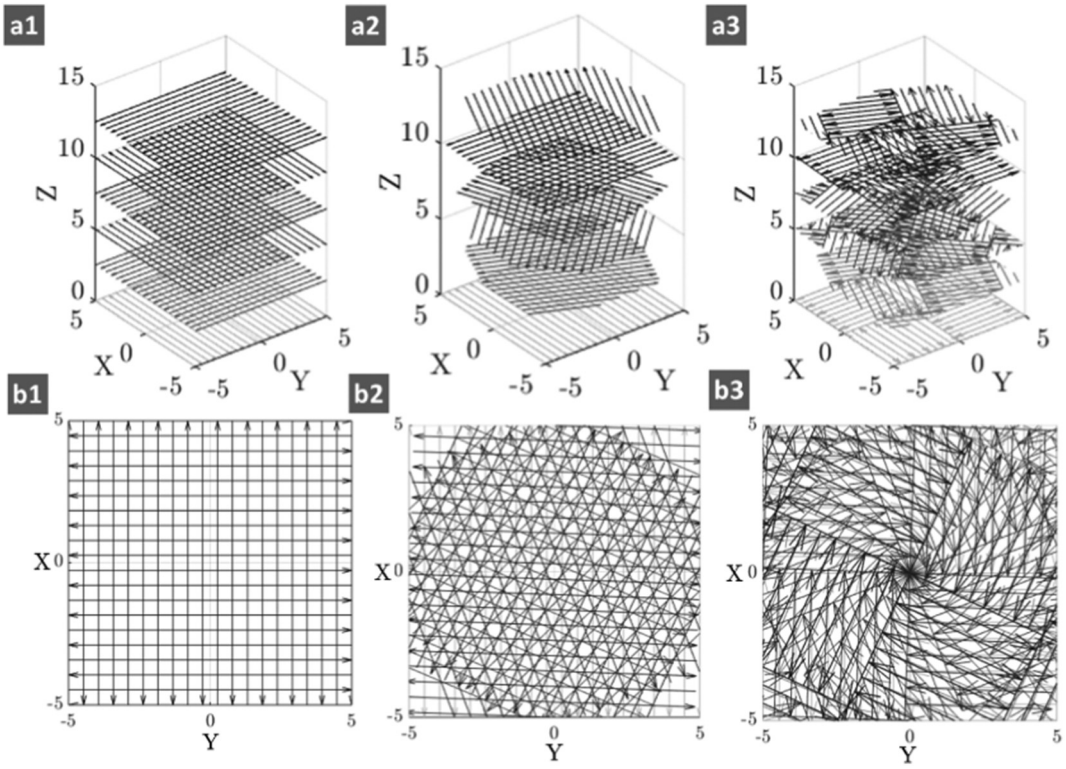

Fig. 7. (a) Scanning directions across six consecutive layers for three scan patterns: 1 -Meander 90° rotation, 2 - Meander 67° rotation and 3 – Chessboard. (b) Corresponding top views. Note that units on the X and Y axes are in mm.

It is worth noting that grains in samples built by the strategy 22 (chessboard with 67° rotation) appear to grow helically when observed both in the Z-section, Fig. 6g, and in the X-section, Fig. 6h, resembling a spiral microstructure as presented in a previous study [28]. The spiral microstructure has dominant grains with [011] orientation aligned with the build direction (Fig. 6g and h). To explore this further, multiple EBSD scans of adjacent areas were carried out at the centre of the Z-section of this sample (as shown in Fig. 8a), and subsequently stitched together. The spiral arrangement of grains becomes very evident on the large EBSD map (Fig. 8b).

Texture data were obtained by combining EBSD data from X- and Z-cuts and are plotted as pole figures in Fig. 9. For strategy 22 only, data from Fig. 8b was used to construct the pole figures instead of Fig. 6g, as the larger area scanned allowed a more representative texture analysis. The strategy 21, Fig. 9a, leads to two dominating sets: the first set has all three ⟨100⟩ aligned to BD, X and Y, while the second one only has one ⟨100⟩ aligned with the single scanning direction Y but the other two inclined at about 45° with respect to the BD, making a ⟨101⟩ parallel to the BD (Fig. 9a). This is consistent with the two alternating sets of orientation reported in our previous study [12]. The shared ⟨100⟩ orientation along the scan direction between the two sets is due to the fact that the laser beam induces crystal growth nearly parallel to the beam direction Y, in particular in the tail of the melt pool. In contrast, strategy 23, Fig. 9c, resulted in a single set of preferred orientations whose three ⟨100⟩ were well aligned with BD, X and Y (note that X and Y were the two alternating scanning directions), i.e. similar to a Cube crystallographic texture. The 67° rotation of the scan pattern in

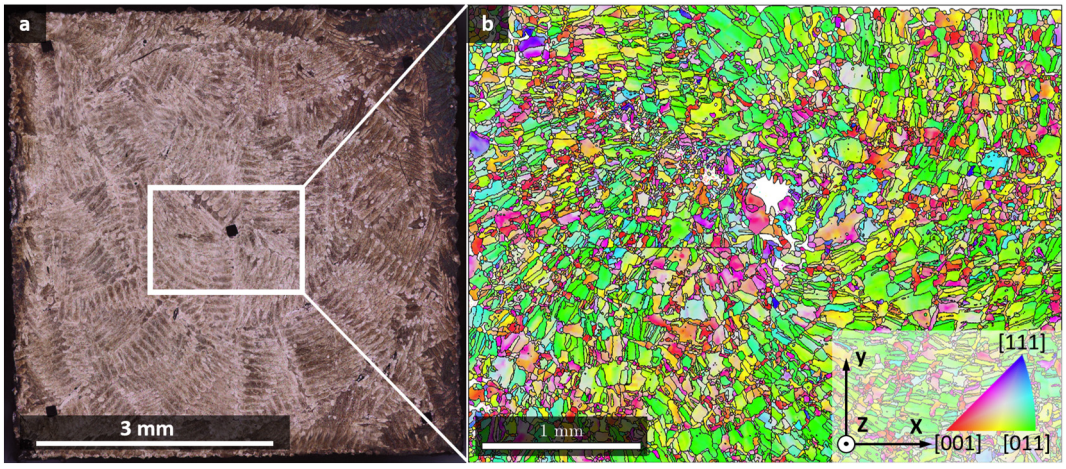

Fig. 8. (a) Optical micrograph of the Z-cut of the sample printed with strategy 22 - chessboard 67 (b) IPF-Z EBSD map of the outlined region in (a). Note that the black region in the centre of (a) is the location of an indent for hardness testing.

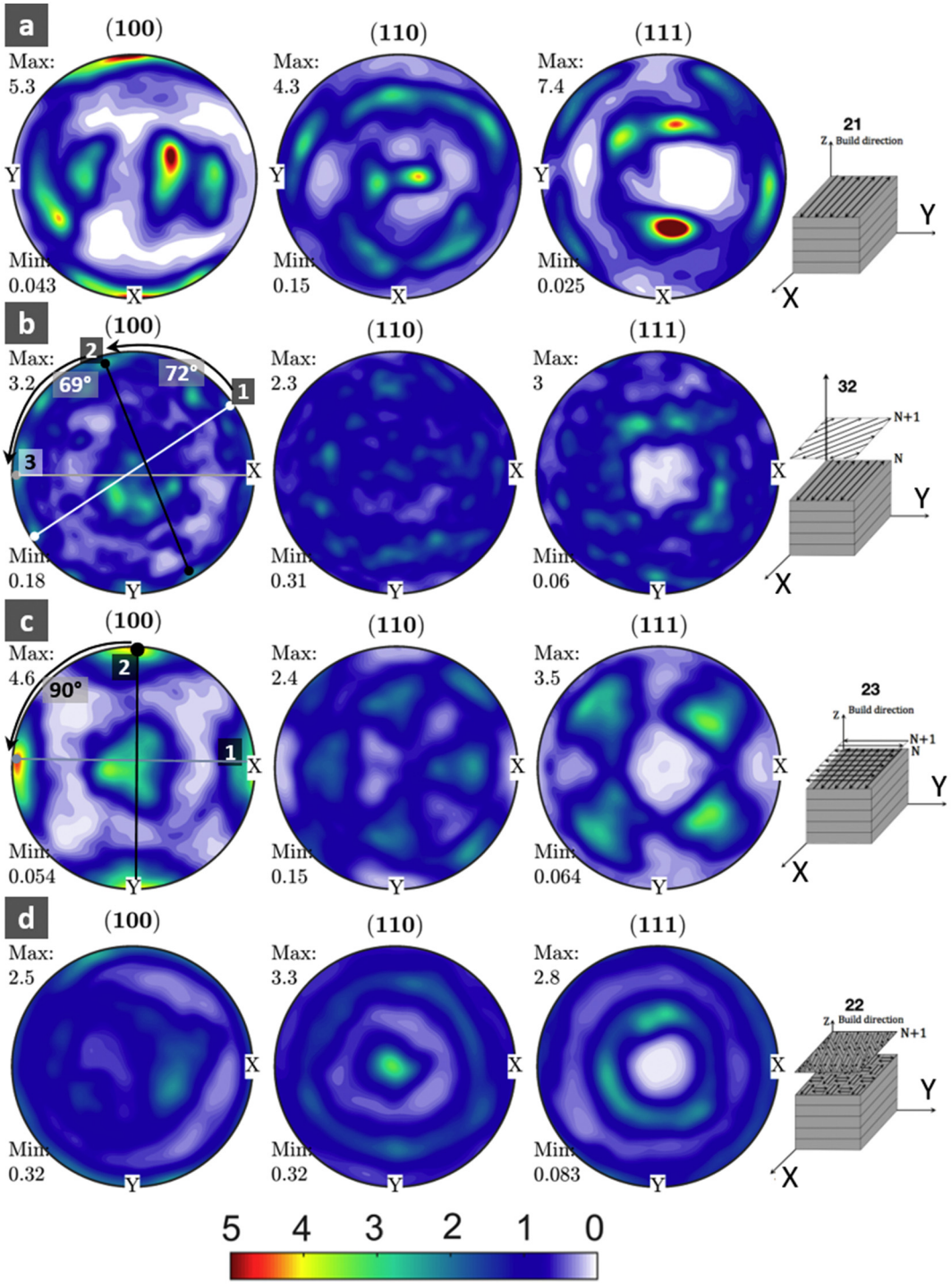

Fig. 9. Pole figures of samples printed with selected scan strategies, obtained from EBSD data of Fig. 6. (a) - strategy 21, (b) - strategy 32, (c) - strategy 23 and (d) - strategy 22.

subsequent layers (Strategy 32-meander and 22-chessboard) resulted in a more random texture, Figs. 9b and d, respectively.

Intuitively, following the observations above about epitaxial growth and heat flux directions, the more repetitive the same scan pattern, the stronger the preferred orientation (i.e., texture). Hence, amongst all the considered strategies, strategy 21 (meander with 0° rotation) results in the strongest texture. In fact, considering the (110) and (111) pole figures of the respective strategies, seen in Fig. 9, the multiple of uniform density (MUD) of texture induced by strategy 21 is almost exactly double that of the 23. It is found that strategy 21 induces a strong (100) fibre texture along the scanning direction, Fig. 9a, while strategy 23 forms two (100) fibre textures, along the two scanning directions at 90° with each other (Fig. 9c). The 67° rotation of patterns in strategies 22 and 32 induces more random texture (Fig. 9(b, d)). In particular, strategy 32 induces fourteen evenly spaced strong peaks on the outer ring of the (100) pole, Fig. 9(b); six of such peaks are marked with dots connected by a line. The angle between the sets of peaks is measured to be ~60–75°, consistent with the 67° rotation between layers. Therefore, such peaks in the pole figures are likely the consequence of the 67° rotations of the bi-directional scan pattern in consecutive layers and the consequent development of fibre texture along the scanning direction in each layer. Finally, strategy 22 produced full rings (Fig. 9d), reflecting the spiral microstructure seen in Fig. 8. The differences in microstructure between strategies 32 (bidirectional scanning) and 22 (chessboard) is

quite pronounced. Both strategies involve a scan pattern rotation of 67°, but strategy 22 includes islands in each layer whose scanning directions are rotated by 90° with respect to neighbouring ones of the same layer. The in-layer rotation of scanning direction by 90° promotes the in-layer epitaxial growth including side-branching across the boundaries between adjoining islands. For example, Fig. 10 shows clear evidence of epitaxial growth including side-branching of grains across two orthogonal tracks of neighbouring islands in a layer of the chessboard pattern (inset of Fig. 10). This enables the grains to extend through several islands, broadening the grain size in the direction perpendicular to the BD [28]. The rotation between layers by 67° can result in an effective angle of 23° between scan tracks between two adjoining islands of two consecutive layers (note that tracks between in-layer chessboard islands are oriented at 90° to each other). This angle is well within a deflection angle limit (found to be ~30°) within which the cells can follow to grow epitaxially without changing their growth direction across consecutive layers, promoting out-of-layer epitaxial growth [28,29]. As this process continues through several layers, a spiral pattern emerges, Figs. 7b3 and 8b as discussed in our previous publication [28].

3.2.4. Scan strategy and grain size

Different scan strategies led to different grain morphologies and orientations with respect to the build direction. However, a common characteristic is that columnar microstructures with elongated grains along the Z (build) direction were seen for all scan patterns (right column of Fig. 6). Consequently, the aspect ratio of the grains sections along the BD direction was found to be consistently higher with respect to the grains sections perpendicular to BD, as shown in Fig. 11a–d. Fig. 11 reveals that strategy 21 results in the most columnar grains, followed by strategy 22, while strategies 23 and 32 were distinctly less columnar. Grain size distributions for the selected samples are shown in Fig. 11e. Cumulative frequency plot reveals that strategy 22 results in the largest average grain size, followed by 32, 23, and 21 respectively.

Both strategies 32 (bidirectional scanning) and 22 (chessboard) involve a scan pattern rotation of 67°, but strategy 22 promotes strong in-layer and out-of-layer side-branching, as previously discussed. The strong in-layer and out-of-layer epitaxial growth results in a substantial broadening of grains and reducing the degree of vertically columnar grains in the chessboard pattern. In the absence of islands in the 67°-meander strategy, the in-plane and out-of-plane epitaxial growth transverse to the BD are limited, resulting in smaller grains in the strategy 32. This explains why strategy 22 shifts the cumulative frequency of grain size towards higher values compared to that of the meander with the same 67° rotation, Fig. 11e. The rotation of the scan pattern by 90° (strategy 23) further reduced the overlapping between the deposited tracks of two consecutive layers, leading to finer grains. Assuming the ideal condition in which every new melt pool lines up perfectly on top of the one lying beneath it for the strategy 21 (no rotation between consecutive layers), the confined out-of-plane epitaxial, but directional growth along the stacking direction of melt track (i.e. build direction) is favoured, leading to the most elongated yet predominantly thin grains. As the grain size is one of the main contributors to the mechanical properties, the understanding of crystal growth in various scan strategies offers more confidence in controlling the average grain size to tailor the mechanical response of the material.

3.3. Mechanical properties

The hardness of samples fabricated using the nine considered printing strategies was measured to study the effect of print parameters on the mechanical properties, and in particular on plastic anisotropy. The results of the hardness measurements are shown in Fig. 12. Hardness results deviate by <10% from the overall average value across all measured

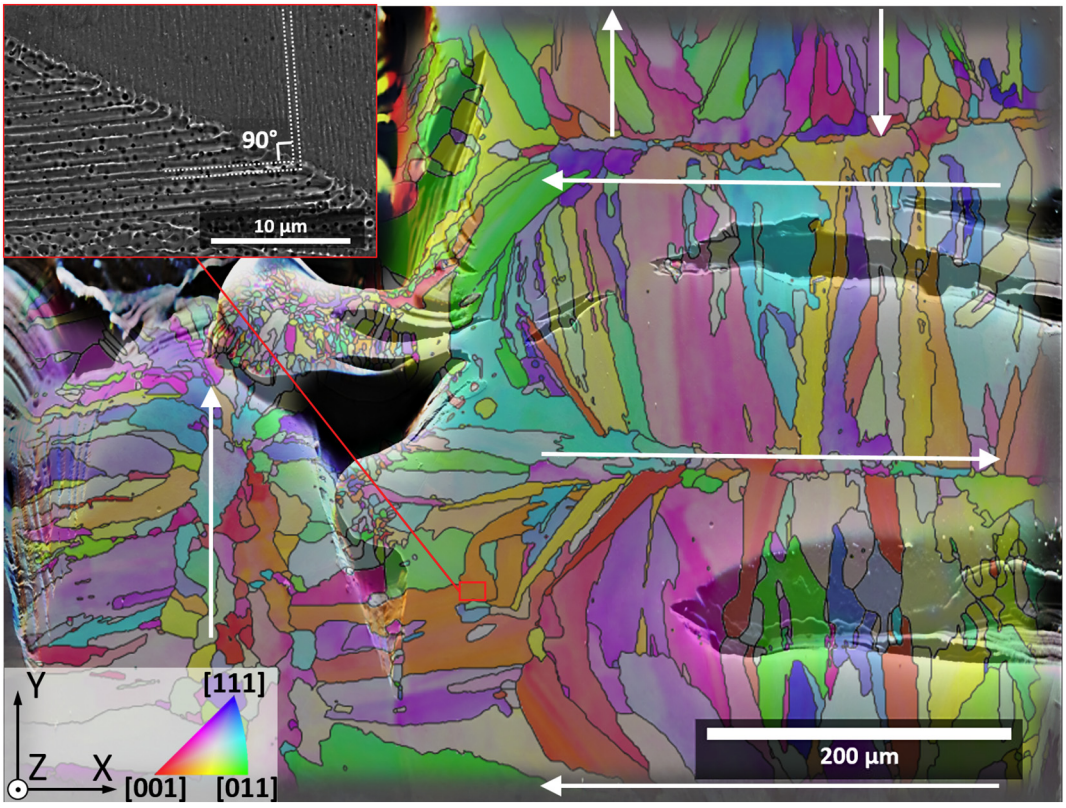

Fig. 10. EBSD IPF-Z map of the top-most layer of the sample fabricated using the chessboard pattern (strategy 22) overlaid onto the SEM image of the semi-polished top-most layer. The Z direction is the build direction. The white arrows indicate the scanning direction of the three adjoining islands. Inset: SEM micrograph of the same location showing evidence of 90° side branching across a fusion boundary.

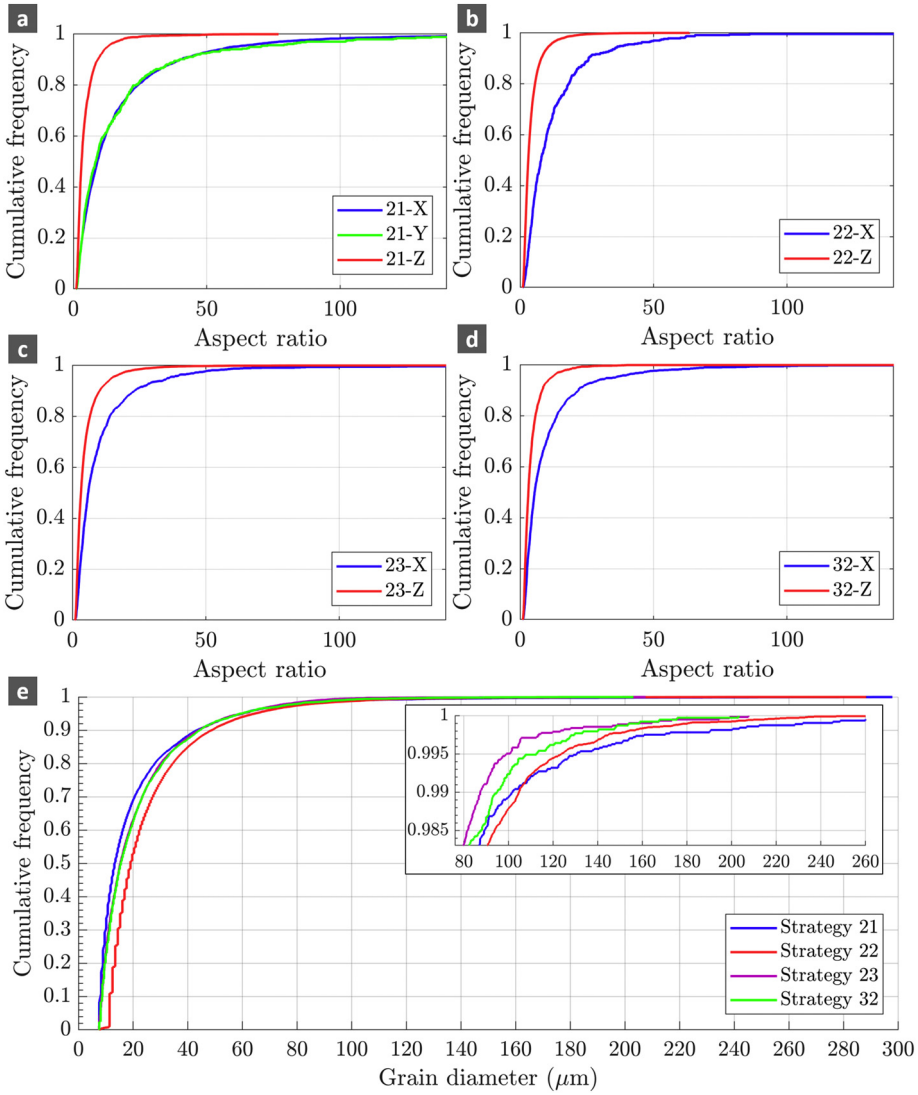

Fig. 11. Grain morphology (size and shape) obtained from EBSD data of Fig. 8. (a)–(d) – cumulative frequency of aspect ratio of grains, (e) – cumulative frequency of the grain sizes resulting from scan strategies 21,22,23 and 32.

samples and are over 40% higher than those of as-cast samples of the same alloy reported by Zhu et al. [30] (as-cast hardness is reported to be 153 HV). There are two trends of interest. Firstly, for each printing strategy, the measurements consistently show a difference between the hardness measured in *Z*-sections, on which the loading direction (LD) was parallel to the build direction, and that measured in X-sections, on which the LD was perpendicular to the build direction, Fig. 12(a). In other words, strong anisotropy is seen in all the samples with the sample 23 fabricated by the meander 90° rotation exhibiting the least anisotropy. Secondly, the hardness measurements do not correlate well with the density measurements carried out on the same sections, Fig. 12(b). The sample with the highest measured relative density (measured using Archimedes' method) was only the 6th hardest (in both sections), and the sample with the lowest measured density was 2nd hardest along the X-section. This may be due to the fact that the indentations are limited to small regions that might not be representative of the entire build. However, hardness was measured at multiple regularly gridded locations on the same section to achieve better representation of the material strength. In addition, hardness is also strongly affected by the microstructure, such as crystallographic texture and grain size. The effect of the microstructure is most reflected in the observed plastic anisotropy. As previously shown, different scan strategies have a considerable effect on microstructures, and consequently on hardness. This can be observed by analysing the hardness of samples fabricated with the same energy densities, but different scan strategies (samples 21, 22, 23 and 32), inset of Fig. 12a. These samples show noticeable differences in hardness despite having very similar consolidation, confirming the resulting microstructure is responsible for the plastic anisotropy observed in hardness measurements.

To study the deformation behaviour of the alloy in tension and compare it with data from the same alloy fabricated by other processes, tensile stress-strain curves of cylindrical test pieces fabricated by the strategy 22 with the sample axis oriented perpendicular to the BD are presented in Fig. 13, along with data for the same HEA made by casting followed by rotary swaging and recrystallisation [31]. The stress-strain data obtained in the current work were highly reproducible and consistent. The total strain was in the range between 22% and 24%. Samples showed initiation of necking at around 20% true strain, with local strain in the necking region reaching over 40%, Fig. 13b and Video S1 (in the Supplementary information). The yield strength (Table 2) of the HEA tensile sample with testing axis perpendicular to the BD was higher than that when loading along the build direction, confirming the anisotropy seen in the hardness measurement, Fig. 12. It should be noted that the yield stress for vertically built samples was extracted from the mechanical data from the first cycle of fatigue tests, performed at the same strain rate as the tensile tests in this study; hence, the data for

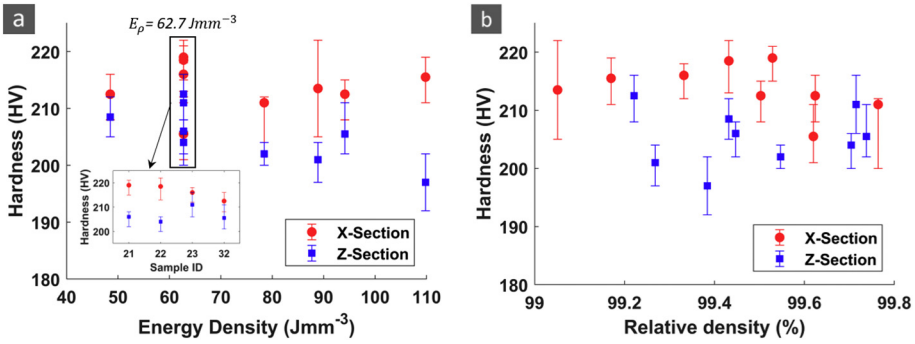

Fig. 12. Hardness of printed samples measured on Z-sections (cut perpendicular to the build direction) and on X-sections (parallel to the build direction) with respect to the energy density (a) and relative density measure by Archimedes' method (b). The error bars represent the 25th and 75th percentile of the measurements. The inset of figure (a) reveals the hardness for different samples with the same energy density.

ultimate tensile strength and ductility is absent for these samples. The mechanical properties of the same alloy reported in previous studies (refs [11,31–33]) were also included in Table 2. The yield stress measured in this study is consistent with a previously reported value for the same alloy fabricated by LPBF [11], and is more than double compared to those reported for the same alloy fabricated by other processes [11,31–33]. The ultimate tensile strength is >33% higher compared to those of samples manufactured by spark plasma sintering (SPS) and vacuum arc remelting (VAR) [32,33].

The fracture surface of the sample (Fig. C1 in Appendix) showed clear signs of dimples suggesting ductile fracture. Several defects were observed (Fig. C1a), mainly lack of fusion and keyhole pores (Fig. C1b). Despite the presence of these defects, the samples showed consistent behaviour and remarkable strength and ductility (Fig. 13a).

3.4. Relationship between microstructure and mechanical properties

The high entropy alloy made by powder-bed fusion consisted of very fine cells (about 700 nm in diameter, Fig. 7(b)). High thermal gradients and rapid cooling in LPBF result in the generation of high dislocation densities as seen in Fig. 5c and d. Dislocation forests at cell boundaries can act as effective obstacles to the movement of dislocations. Hence, the presence of fine cells results in a significant improvement in the macroscopic flow stress of the alloy made by LPBF, explaining the high hardness (Fig. 12) and yield stress (Fig. 13) compared to the same alloy made by other processes, as shown in Table 2.

The HEA in this study exhibits strong anisotropy, regardless of the print parameters used – as highlighted by differences in both the hardness (Fig. 12) and tensile properties measured along the directions parallel and transverse to the BD (Table 2) in consistent with our previous report [28]. Fig. 12(b) suggests that the porosity of the investigated sections is not the reason behind such differences. It is known that

Table 2
Tensile properties of the CoCrFeMnNi high entropy alloy measured in this study (LPBF) compared to those reported in previous studies. (VAR - vacuum arc remelting, SPS - spark plasma sintering).

Sample state	Yield stress (0.2% offset (MPa)	UTS (MPa)	Strain at break (%)	Ref
LPBF (X-direction)	530 ± 20	783 ± 7	23 ± 1	This
LPBF (Z-direction)	455 ± 10	N/A	N/A	study
LPBF (X-direction)	519 ± 20	500–601	22–34	[11]
VAR + drop-casting	210	590	42	[32]
SPS	237–312	571–613	27–37	[33]
Rotary swaging + recrystallization	265 ± 10	740	31	[31]

crystallographic texture and grain morphology are influential to the plastic anisotropy [10]. Figs. 6, 9, and 11 show that texture and grain morphology induced by the four considered scan strategies are distinctively different from the others. In the following, the contribution associated with crystallographic texture and grain morphology to the observed anisotropy is discussed in detail.

Concerning the effect induced by texture, plastic deformation is easier in grains where the slip systems are well aligned with the maximum shear stress (i.e. high Schmid factor) and harder in grains where slip systems are not favourably aligned with the maximum shear direction (i.e. low Schmid factor). Therefore, the crystallographic orientations of the grains control the apparent yield stress of the material. The Taylor factor is a common way to quantify the influence of crystallographic orientations on the macroscopically measured yield stress of the material, Eq. (4):

$$\sigma_y \propto \overline{M}\tau_{crss} \tag{4}$$

where τ_{crss} denotes the critical resolved shear stress and $\overline{M}$ is the average Taylor factor of a polycrystalline material, defined by Eq. (5):

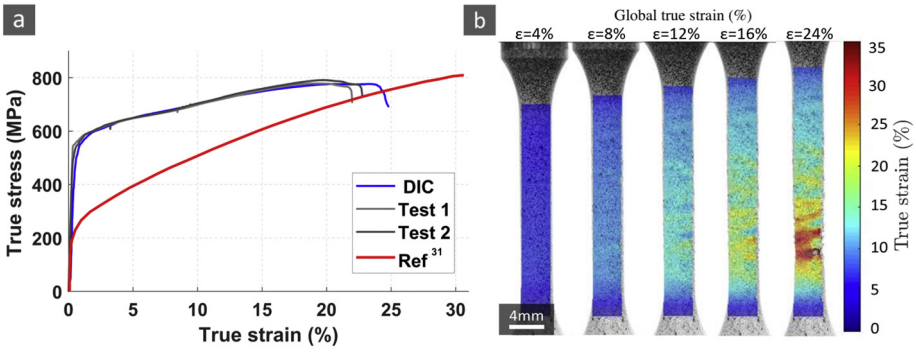

Fig. 13. (a) Tensile stress-strain curves for horizontally built HEA test pieces and (b) corresponding DIC image sequence at different strain levels of the HEA fabricated by LPBF. (Data of the red curve was obtained from ref [31]). (For interpretation of the references to color in this figure legend, the reader is referred to the web version of this article.)

$$\overline{M} = \sum_{j=1}^{m} f_j M_j \tag{5}$$

where f_j is the distribution function of the orientation of grain j with respect to the loading direction, M_j is the Taylor factor of the orientation j, and m is the total number of orientations. Higher Taylor factor usually leads to higher flow stress and higher hardness. MTEX Toolbox was used to calculate the Taylor factor based on measured crystallographic orientations (Fig. 9) for two conditions: loading direction is either perpendicular or parallel to the build direction (i.e., X section or Z section, respectively). Fig. 14(a) clearly shows that the Taylor factor when loading on the X-section is larger than that on the Z-section in all samples; this explains why a higher flow stress of the X-sections is observed in the hardness measurements.

However, the crystallographic texture alone does not explain the variation in hardness measured along the same loading direction between samples fabricated by different scan strategies. For example, for the hardness measurements on Z-sections, sample 23 exhibits the highest values despite having the lowest Taylor factor, Fig. 14a. The variation in hardness along the same loading direction between different scan strategies could be associated with dislocation distribution, distinct cell morphologies (Fig. 5c and d), and grain morphology (Figs. 6, 11). Because of side-branching, the distribution of cell morphological orientations and dislocation densities along and orthogonal to the BD is statistically rather similar. In addition, the length of the indented regions was about 200 μm (Fig. 8a), much larger than the cell size (measured to be about 700 nm for all strategies). Furthermore, the dislocation densities in samples fabricated by 21, 22, 23, and 32 strategies, characterised by the same energy density, are expected to be not much different. It follows that the grain morphology (Fig. 11e) is likely to be the cause for the differences in hardness in samples fabricated with distinct scan strategies; this argument is supported by the fact that grains are on a similar scale as the indenter tip. The grain morphology can be quantified by the grain size measured along different directions either parallel or perpendicular to the BD. The contribution of grain size to the flow stress due to hardness indentation can be accounted for using the Hall-Petch relationship [34], Eq. (6):

$$\sigma_y \propto D_{av}^{-\frac{1}{2}} \tag{6}$$

In which D_{av} stands for average grain size measured in a specific direction (either parallel or perpendicular to the build direction). Fig. 14b shows the plot of $D_{av}^{-\frac{1}{2}}$ against the average hardness measured on X and Z sections of the investigated samples. The trend line confirms that the grain size plays a significant role in the hardness of the samples. For example, sample 22 had the largest average grain size and hence displays the lowest hardness on the Z-section. Similarly, sample 23 had the smallest average grain size, therefore resulting in the highest hardness on the Z-section. The combined effect of crystallographic texture and grain size provides reasonable explanations for the hardness trends observed.

The obtained findings of the relationships between consolidation, solidification microstructure, and mechanical properties of this alloy provide crucial knowledge to control the microstructure to specific locations with improved confidence, hence achieving site-specific tailored properties. In particular, these findings form a basis for future additive manufacturing of the alloy with desired anisotropy or isotropy. For example, to achieve the isotropy, it is recommended to use the meander 90° rotation as this scan strategy results in a cube-like texture which induces the most isotropic property next to a random crystallographic texture [35]. However, an optimal for both isotropic properties and consolidation, the chessboard 67° rotation should be considered.

4. Conclusions

This study assesses the printability including the consolidation, solidification microstructure, and mechanical properties of the CoCrFeMnNi high entropy alloy fabricated by Laser Powder Bed Fusion. This comprehensive assessment provides a basis to establish the relationship between processing parameters, microstructure, and mechanical properties for this alloy. It was shown that the alloy can be fabricated with high consolidation using an energy density ranging from 62.7 to 109.8 kJ/m^3. However, it was found that the consolidation does not exclusively depend on the processing parameters (i.e. laser power, scan speed, hatch spacing and layer thickness) that constitute the energy density and are typically tailored for porosity minimisation; in fact, the scan pattern also plays an important role in the consolidation of the builds. For the same energy density, a 67° rotation of consecutive layers tends to induce higher consolidation. Moreover, the scan patterns were found to have a profound influence on the grain morphology and crystallographic textures developed in printed parts. In particular, the rotation angle between the scan patterns of consecutive layers was found to be crucial, as it influences the relative orientation of the heat gradients of a new melt pool with respect to those of previously solidified tracks. The rotation angle between consecutive layers controls the extent to which epitaxial growth (in particular the side-branching) can occur, and hence the crystallographic texture and the morphology of grains developed in the build. Amongst the four considered strategies, the 0° and 90° rotations lead to the strongest and second strongest preferred texture, while the 67° rotation results in weaker texture. The developed textures are responsible for plastic anisotropy

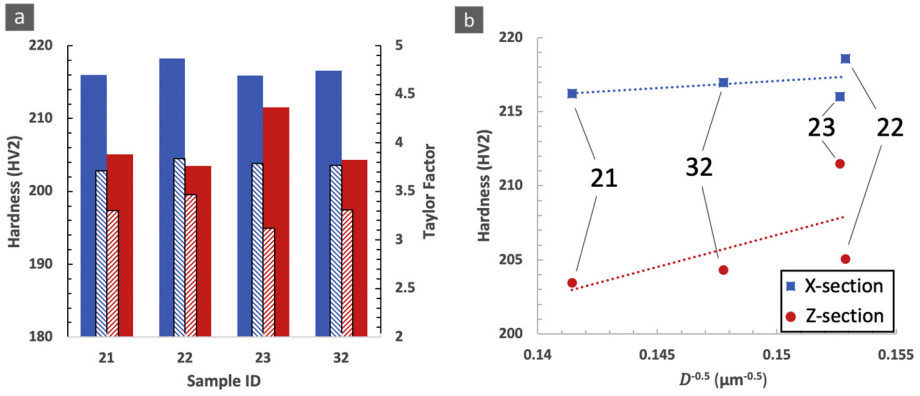

Fig. 14. (a) Effect of scan strategy on hardness (large solid bars) and Taylor factor (small dashed bars) of samples with different scan strategies measured transverse (blue) and parallel (red) to the build direction. (b) Effect of the grain size on the average hardness along the X and Z sections with a linear trend line (parallel and perpendicular to Build direction respectively; note the labelled Sample IDs). (For interpretation of the references to color in this figure legend, the reader is referred to the web version of this article.)

with the meander 90° rotation inducing the least anisotropy, as observed in hardness and tensile tests. In addition to the effect on crystallographic texture, the chessboard strategy with the 67° rotation resulted in the most broadened grains, with the lowest aspect ratio, i.e. least columnar. Different grain sizes also contribute to variations in flow stress, explaining the variation of hardness in samples fabricated by different scan strategies.

Supplementary data to this article can be found online at https://doi.org/10.1016/j.matdes.2020.108845.

CRediT authorship contribution statement

Bogdan Dovgyy: Conceptualization, Methodology, Software, Investigation, Writing - original draft, Writing - review & editing, Visualization. **Alessandro Piglione:** Conceptualization, Investigation, Writing - review & editing. **Paul A. Hooper:** Resources, Writing - review & editing. **Minh-Son Pham:** Conceptualization, Supervision, Writing - review & editing, Funding acquisition.

Acknowledgment

The authors would like to thank Tobias Ronnenberg for the assistance in tensile testing. Also, the authors would like to acknowledge the EPSRC for supporting the research (grant EP/K503733/1).

Data availability

The raw/processed data required to reproduce findings reported in the current study are available from the corresponding author on reasonable request.

Declaration of competing interest

The authors declare that they have no known competing financial interests or personal relationships that could have appeared to influence the work reported in this paper.

Appendix A. Appendix

Table A1
Composition of the High Entropy Alloy powder measured through EDX and as stated by the supplier.

Element	Nominal composition (at. %)	EDX composition (at. %)	EDX composition (wt%)	Composition stated by supplier (wt%)
Cr	20	19.6	18.14	18.20
Mn	20	18.2	17.79	17.90
Fe	20	19.5	19.38	19.50
Co	20	22.3	23.39	23.20
Ni	20	20.4	21.31	21.20

Section A

(This section is based on the theories of heterogeneous nucleation and competitive growth presented in a text book authored by Dantzig and Rappaz ref. [36])

Assuming that a nucleus solid (which is a spherical cap) present at the interface of liquid and a pre-existing solid and all surface energies are isotropic, the contact angle (θ) is related to surface energies (Fig. A1a) as follows:

$$\gamma_{ml} = \gamma_{sm} + \cos\theta\gamma_{sl} \tag{A1}$$

Rearranging, gives:

$$\cos\theta = \frac{\gamma_{ml} - \gamma_{sm}}{\gamma_{sl}} \tag{A2}$$

where γ denotes surface energy, the subscripts denote the involved medium (m: pre-existing solid (i.e. metallic substrate), s: solidifying nucleus and l: liquid). Assuming that the nucleus has almost identical composition to that of the pre-existing metal which is usually the case in additive manufacturing, then $\gamma_{sm} \approx 0$ and $\gamma_{ml} \approx \gamma_{sl}$; therefore, θ~0.

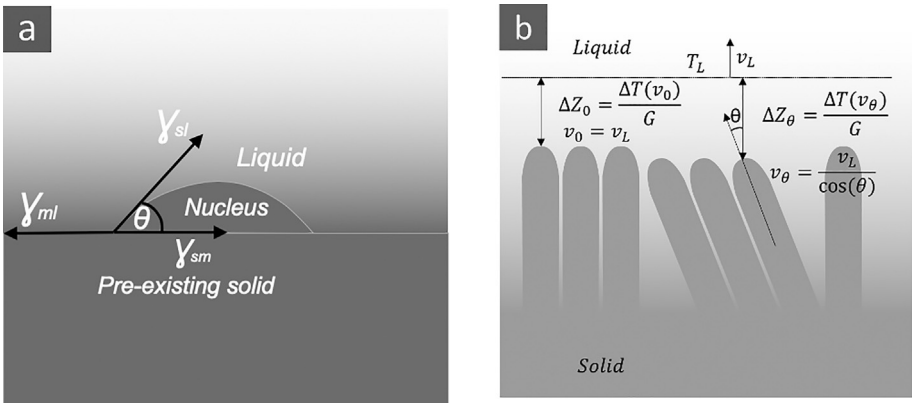

Fig. A1. (a) Contact angle (θ) and surface tensions in the presence of a solid nucleus at the interface between liquid and a pre-existing solid (b) Competitive growth of crystals. (Adapted from ref. [1]).

In addition, the Gibbs free energy change (ΔG) associated with the presence of the solid nucleus:

$$\Delta G = f(\theta)\left\{4\pi r^2\gamma_{sl} - \Delta S_f^m \Delta T \frac{4}{3}\pi r^3\right\} \tag{A3}$$

where $f(\theta) = \frac{2-3\cos\theta+\cos^3\theta}{4}$, ΔS_f^m is the molar entropy of fusion, T is temperature and r is the radius of the spherical cap.
Minimizing ΔG with respect to r gives the energy barrier (i.e. minimum driving force) for nucleation of grains is:

$$\Delta G^* = f(\theta)\frac{16\pi}{3}\frac{{\gamma_{sl}}^3}{\left(\Delta S_f^m \Delta T\right)^2} \tag{A4}$$

If $\theta = 0, f(\theta) = 0$: there is no nucleation. The solidification of liquid metal is governed by growth.
Within each melt pool, the growth of multiple cells of different orientations inevitably leads to growth competition. In turn, growth competition is governed by the alignment of cells with respect to the heat flux (Fig. A1b). Say, a liquidus isotherm, T_L, travels at a velocity, v_L. Assuming flat isotherms, the cells misaligned at an angle θ grow at a velocity, $v_\theta = \frac{v_L}{\cos(\theta)}$, while cells aligned with the thermal gradient grow at the speed of the liquid isotherm $v_0 = v_L$. This means that the misaligned cells should grow faster than the aligned one. Because the cell tip undercooling increases with velocity, meaning that inclined cells experience greater undercooling, i.e. $\Delta T(v_\theta) > \Delta T(v_0)$. This requires the distance of the tip of misaligned cells to the liquid isotherm (ΔZ_θ) to be larger than that of the aligned cells (ΔZ_0), i.e. the tip of misaligned cells should be behind that of aligned ones. As the misaligned cells lag behind, their path gets blocked by better aligned ones.

Section B

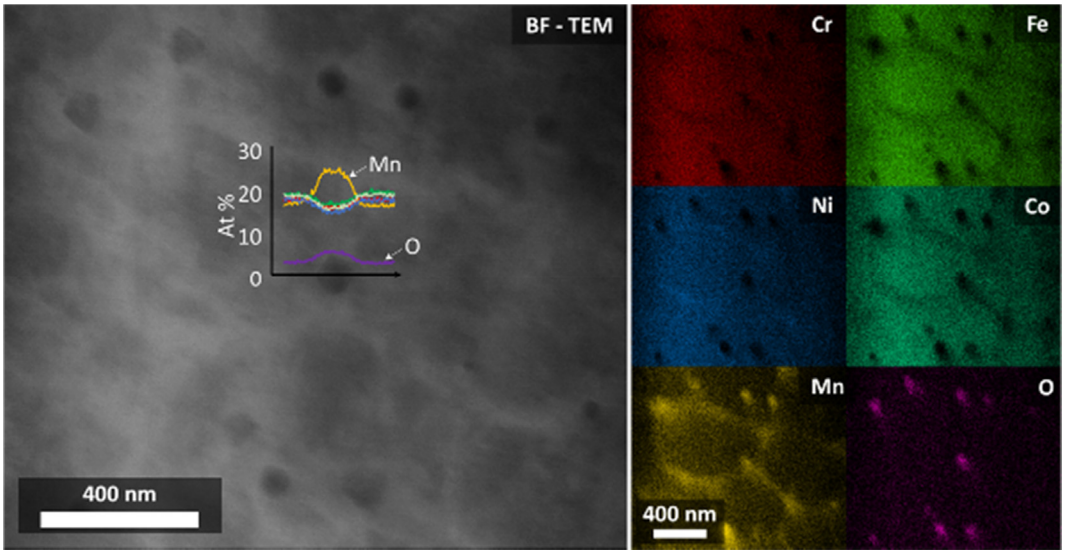

Fig. B1. Bright Field Scanning Transmission Electron Microscopy (BF-STEM) image of High Entropy Alloy, with line profile EDX – STEM through an observed precipitate, along with elemental mapping of the same region.

Section C

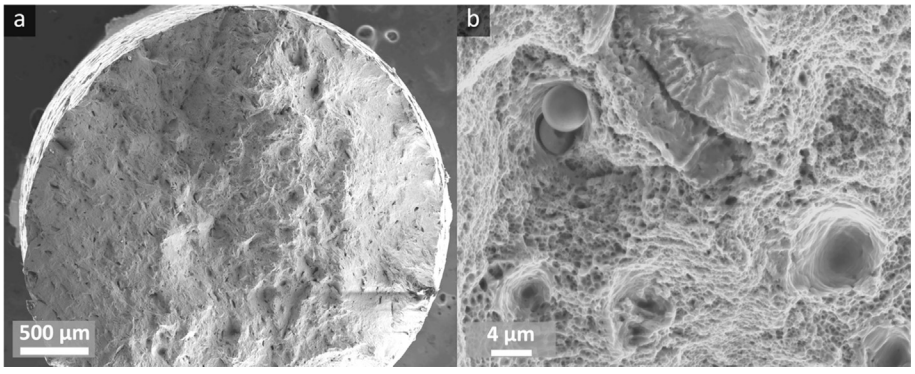

Fig. C1. (a) Micrograph of a facture surface of the DIC sample (refer to Fig. 13). (b) a zoom-in area of the fracture surface showing dimples, suggesting ductile fracture.

References

[1] Royal Academy of Engineering, Additive manufacturing : opportunities and constraints, R. Acad. Eng. (2013) 21 no. May 2013.

[2] M.-S. Pham, C. Liu, I. Todd, J. Lertthanasarn, Damage-tolerant architected materials inspired by crystal microstructure, Nature 565 (7739) (2019) 305–311 Jan.

[3] A. Kudzal, et al., Effect of scan pattern on the microstructure and mechanical properties of Powder Bed Fusion additive manufactured 17-4 stainless steel, Mater. Des. 133 (2017) 205–215.

[4] F. Geiger, K. Kunze, T. Etter, Tailoring the texture of IN738LC processed by selective laser melting (SLM) by specific scanning strategies, Mater. Sci. Eng. A 661 (2016) 240–246.

[5] T. Ishimoto, K. Hagihara, K. Hisamoto, S.H. Sun, T. Nakano, Crystallographic texture control of beta-type Ti–15Mo–5Zr–3Al alloy by selective laser melting for the development of novel implants with a biocompatible low Young's modulus, Scr. Mater. 132 (2017) 34–38.

[6] L. Thijs, M.L. Montero Sistiaga, R. Wauthle, Q. Xie, J.P. Kruth, J. Van Humbeeck, Strong morphological and crystallographic texture and resulting yield strength anisotropy in selective laser melted tantalum, Acta Mater. 61 (12) (2013) 4657–4668.

[7] V. Livescu, C.M. Knapp, G.T. Gray, R.M. Martinez, B.M. Morrow, B.G. Ndefru, Additively manufactured tantalum microstructures, Materialia 1 (2018) 15–24 Sep.

[8] S.-H. Sun, K. Hagihara, T. Nakano, Effect of scanning strategy on texture formation in Ni-25 at.%Mo alloys fabricated by selective laser melting, Mater. Des. 140 (2018) 307–316 Feb.

[9] Y. Kok, et al., Anisotropy and heterogeneity of microstructure and mechanical properties in metal additive manufacturing: a critical review, Mater. Des. 139 (2018) 565–586.

[10] H.R.W.U.F. Kocks, C.N. Tome, Texture and Anisotropy: Preferred Orientations in Polycrystals and Their Effect on Materials Properties, Cambridge University Press, 2000.

[11] R. Li, P. Niu, T. Yuan, P. Cao, C. Chen, K. Zhou, Selective laser melting of an equiatomic CoCrFeMnNi high-entropy alloy: Processability, non-equilibrium microstructure and mechanical property, J. Alloys Compd. 746 (2018) 125–134 May.

[12] A. Piglione, B. Dovgyy, C. Liu, C.M. Gourlay, P.A. Hooper, M.S. Pham, Printability and microstructure of the CoCrFeMnNi high-entropy alloy fabricated by laser powder bed fusion, Mater. Lett. 224 (2018) 22–25 Aug.

[13] J.P. Oliveira, et al., Gas tungsten arc welding of as-rolled CrMnFeCoNi high entropy alloy, Mater. Des. 189 (2020), 108505. Apr.

[14] J. Guo, M. Goh, Z. Zhu, X. Lee, M.L.S. Nai, J. Wei, On the machining of selective laser melting CoCrFeMnNi high-entropy alloy, Mater. Des. 153 (2018) 211–220 Sep.

[15] X. Zhou, et al., Textures formed in a CoCrMo alloy by selective laser melting, J. Alloys Compd. 631 (2015) 153–164.

[16] P. Wang, et al., Additively manufactured CoCrFeNiMn high-entropy alloy via pre-alloyed powder, Mater. Des. 168 (2019), 107576. Apr.

[17] C. Haase, F. Tang, M. B. Wilms, A. Weisheit, and B. Hallstedt, "Combining thermodynamic modeling and 3D printing of elemental powder blends for high-throughput investigation of high-entropy alloys – towards rapid alloy screening and design," *Mater. Sci. Eng. A*, vol. 688, no. January, pp. 180–189, 2017.

[18] G. Laplanche, P. Gadaud, O. Horst, F. Otto, G. Eggeler, E.P. George, Temperature dependencies of the elastic moduli and thermal expansion coefficient of an equiatomic, single-phase CoCrFeMnNi high-entropy alloy, J. Alloys Compd. 623 (2015) 348–353 Feb.

[19] F. Bachmann, R. Hielscher, H. Schaeben, Texture analysis with MTEX – free and open source software toolbox, Solid State Phenom. 160 (2010) 63–68.

[20] M. Letenneur, A. Kreitcberg, V. Brailovski, Optimization of laser powder bed fusion processing using a combination of melt Pool modeling and design of experiment approaches: density control, J. Manuf. Mater. Process 3 (1) (2019) 21.

[21] U. Scipioni Bertoli, A.J. Wolfer, M.J. Matthews, J.P.R. Delplanque, J.M. Schoenung, On the limitations of volumetric energy density as a design parameter for selective laser melting, Mater. Des. 113 (2017) 331–340.

[22] A. Basak, S. Das, Epitaxy and microstructure evolution in metal additive manufacturing, Annu. Rev. Mater. Res. 46 (1) (2016) 125–149 Jul.

[23] W.J. Boettinger, et al., Solidification microstructures: recent developments, future directions, Acta Mater. 48 (1) (2000) 43–70 Jan.

[24] W. Kurz, C. Bezençon, M. Gäumann, Columnar to equiaxed transition in solidification processing, Sci. Technol. Adv. Mater. 2 (1) (2001) 185–191 Jan.

[25] M. Gäumann, S. Henry, F. Cléton, J.-D. Wagnière, W. Kurz, Epitaxial laser metal forming: analysis of microstructure formation, Mater. Sci. Eng. A 271 (1–2) (1999) 232–241 Nov.

[26] Z.G. Zhu, et al., Hierarchical microstructure and strengthening mechanisms of a CoCrFeNiMn high entropy alloy additively manufactured by selective laser melting, Scr. Mater. 154 (2018) 20–24 Sep.

[27] Y.M. Wang, et al., Additively manufactured hierarchical stainless steels with high strength and ductility, Nat. Mater. 17 (October) (2017) 63–70 Jan.

[28] M.-S. Pham, B. Dovgyy, P.A. Hooper, C.M. Gourlay, A. Piglione, The role of side-branching in microstructure development in laser powder-bed fusion, Nat. Commun. 11 (1) (2020) 749 Dec.

[29] B. Dovgyy, M.-S. Pham, Epitaxial growth in 316L steel and CoCrFeMnNi high entropy alloy made by powder-bed laser melting, AIP Conference Proceedings, vol. 1960, 2018, p. 140008 , no. 140008.

[30] Z.G. Zhu, K.H. Ma, X. Yang, C.H. Shek, Annealing effect on the phase stability and mechanical properties of (FeNiCrMn)(100−x)Coxhigh entropy alloys, J. Alloys Compd. 695 (2017) 2945–2950.

[31] G. Laplanche, A. Kostka, O.M. Horst, G. Eggeler, E.P. George, Microstructure evolution and critical stress for twinning in the CrMnFeCoNi high-entropy alloy, Acta Mater. 118 (2016) 152–163.

[32] A. Gali, E.P. George, Tensile properties of high- and medium-entropy alloys, Intermetallics 39 (2013) 74–78.

[33] N. Eißmann, B. Klöden, T. Weißgärber, B. Kieback, High-entropy alloy CoCrFeMnNi produced by powder metallurgy, Powder Metall. 60 (3) (2017) 184–197.

[34] Hall, The deformation and ageing of mild steel III discussion of results\t, Proc. Phys. Soc. Sect. B 64 (9) (1951) 747.

[35] M.S. Pham, A. Creuziger, M. Iadicola, A.D. Rollett, Roles of texture and latent hardening on plastic anisotropy of face-centered-cubic materials during multi-axial loading, J. Mech. Phys. Solids 99 (2017) 50–69 Feb.

[36] M. Rappaz, C.A. Gandin, J.L. Desbiolles, T. Thévoz, Prediction of grain structures in various solidification processes, Metall. Mater. Trans. A 27 (1996) 695–705.